energy&fuels

pubs.acs.org/EF

Article

Bed Model for Grate-Fired Furnaces: Computational Fluid Dynamics Modeling and Comparison to Experiments

Nils Erland L. Haugen,* Mette Bugge, Alexander Mack, Tian Li, and Øyvind Skreiberg

Cite This: *Energy Fuels* 2022, 36, 5852−5867

Read Online

ACCESS | Metrics & More | Article Recommendations

ABSTRACT: A detailed but still central processing unit (CPU)-efficient bed model for grate-fired combustion of biomass and waste is developed. Simulations of wood chip combustion are performed, and the results are compared to experiments. The so-called layer model is used to track the development of the thermally thick representative fuel particles in the bed. As an efficient way of handling a large number of physical fuel particles, each representative fuel particle represents a number of physical particles with the exact same properties. The motion of the fuel bed is handled in a way that requires negligible CPU power, while for wastes and other fuels with less defined shapes and structure, it still yields accuracy similar to the much more CPU-intensive collision-based models. In this work, the bed model is coupled with ANSYS Fluent and used to simulate one of the test campaigns performed at the grate-fired pilot unit at the University of Stuttgart. It is found that for the test campaign of interest, burning wood chips, the fuel bed is ignited from below, and it is explained how this is due to the thermal properties of the grate and how important the numerical handling of the grate is for an accurate prediction of the bed behavior.

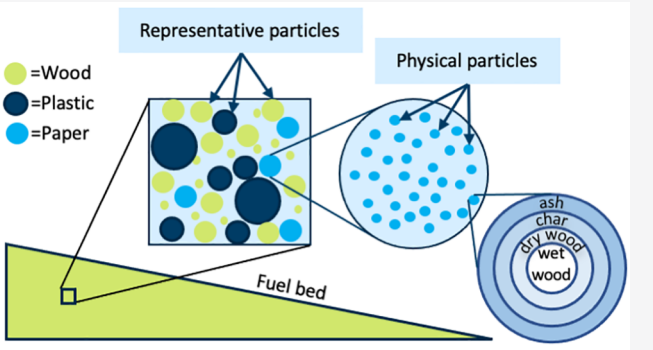

1. INTRODUCTION

Grate-fired biomass-to-energy (BtE) and waste-to-energy (WtE) plants are commonly applied to produce heat and/or power from various types of biomass and waste in plants of different sizes. Such plants are relatively robust and flexible and come in various designs, including for the grate. Dependent upon the feedstock and emission regulations, flue gas cleaning is applied for removal of particles, SO_2, HCl, dioxins, and NO_x. For WtE plants, requirements are put on the flue gas temperature and residence time at this temperature to ensure proper CO burnout. Emission control by primary measures is sought as far as possible, to enhance cost-effectiveness. In this respect, detailed knowledge of the feedstock behavior as it travels along the grate and is gradually converted becomes very interesting. This behavior is influenced by a number of external and internal factors, operational as well as through design; e.g., the grate design and operational principle itself, the primary air addition from below the grate and secondary air addition above the grate, and controlling the freeboard combustion process and its contribution to the radiative force onto the fuel bed are all part of a complex and reactive three-phase fluid dynamic system. Detailed knowledge about this system is useful for improving the combustion process on the grate. Feeding the knowledge into a computational tool, enabling simulations of this combustion process, again enables further knowledge generation and optimization of the grate and the combustion plant operation; e.g., for minimization of NO_x emission by primary measures, CO spikes as a result of combustion instability caused by rapid fuel or operational changes or controlling temperatures to avoid ash-related operational problems.

Resolving all relevant scales, ranging from the smallest chemical or turbulent scale all of the way up to the size of the grate and furnace, is not yet feasible for a commercial plant. Numerical tools that use advanced numerical models that account for all relevant subgrid scale phenomena, such that the computational costs can be kept manageable, are therefore required to study grate combustion plant operation. Such a tool must consist of two main elements: the fuel bed solver, handling the conversion of the solid fuel, and the computational fluid dynamics (CFD) solver, which handles the gaseous flow. The focus of this paper will be on the fuel bed solver and its coupling to the CFD solver but not on the CFD solver itself. In the end, a comprehensive yet central processing unit

Received: December 12, 2021
Revised: May 2, 2022
Published: May 20, 2022

(CPU)-balanced bed model for grate-fired furnaces is proposed. Its theory is presented and a comparison against experimental results is carried out.

A proper fuel bed model consists of two main submodels: the first is a submodel that handles the evolution of the interior of the individual particles in the bed, while the second is a submodel that takes care of particle motions and the interaction between the particles and the surrounding gas phase. There are two main versions of the submodel for individual particles, depending upon whether the particles are considered as thermally thick or thermally thin. For thermally thick particles, temperature gradients exist within the particle, which means that multiple thermal conversion processes may occur simultaneously within a given particle. Such particles are typically solved by use of a layer model,[1] where the particle is divided into four layers, separated by the three boundaries where the thermochemical conversion processes (drying, devolatilization, and char conversion) occur. For thermally thin particles, however, the temperature within the particle is uniform such that the conversion processes occur in series instead of in parallel. This makes the particle treatment easier.

The second part of the fuel bed model, the part that handles the motion of the particles and particle−fluid interactions, is commonly treated with either the Eulerian or Lagrangian approach. In the Lagrangian approach, fuel particles are inserted into the numerical domain and tracked as they move through the domain. In the Eulerian approach, however, every grid point of the fluid mesh is solved with respect to the particle model, while the particle ensemble is treated as a fluid. The motion of the particles is then emulated through the particle properties being transported by the advective term of the Eulerian transport equations.

One of the benefits of the Lagrangian approach for multiphase simulations is that it does not have to be predescribed where the bed is and, hence, in which grid cells one has to solve the particle equations. Instead, the effect of the bed is automatically accounted for wherever there are Lagrangian particles present. Another advantage of the Lagrangian approach is that one can easily, at no extra computational cost, introduce particles of different types for given periods of time. In addition, particles with different sizes can easily be taken into account. This is not the case for the Eulerian approach. As such, the Lagrangian approach is more flexible than the Eulerian approach, but the Eulerian approach may have an advantage when it comes to computational cost if both the particle type and the height of the bed are well-defined and roughly constant in time.

When the Lagrangian approach is applied, it is customary to make sure all particles are in contact at any time. This involves a procedure where every particle in the bed has to determine where the other particles in the bed are before they move (with gravity) such that they come in contact with the closest particle. This approach is very accurate for rigid spherical particles, but it comes at the expense of a significant CPU cost.[2] On top of the high CPU cost, the value of this sophistication will be next to nothing for the case of waste incineration, where particles typically are highly non-spherical and may not even be rigid at the temperatures of interest.

The combination of the layer model with the Eulerian approach for the particles is used extensively by the group of Thunman at Chalmers[3,4] and also by several other groups.[5−7] In the work of Gu et al.,[8] the Eulerian approach is also used, but in this work, the authors assume that the particles are thermally thin, such that the layered particle approach is redundant. It is assumed that thermally thin particles save some CPU time; however, to be valid, it requires that the bed consists of only small particles. In the work of Mehrabian et al.,[9] Zhang et al.,[10] and Somwangthanaroj et al.,[11] the authors use the Lagrangian framework together with the layer model. Wissing et al.[2] also use the Lagrangian approach and solve for collisions between individual particles to determine their motion, but they use the so-called FLIC code to calculate the reactions of individual bed particles. For reviews covering conversion of solid fuels on grates, the reader is referred to refs 12−14.

Given accurate knowledge of the size, shape, composition, and kinetics of the fuel particles, the layer model will yield an accurate representation of thermal fuel degradation, including the corresponding gas release (and consumption). Given that the fuel is shaped into spherical particles that are rigid and non-sticky under the conditions experienced in the fuel bed, the Lagrangian particle tracking model combined with the layer model will therefore be able to provide very reliable simulation results, although the associated CPU costs may be significant. Problems occur, however, when the fuel particles are not spherical, rigid, or non-sticky. This is typically the situation for combustion of wastes. Then, the Lagrangian particle tracking model will not be able to provide a reasonable representation of the movement of the fuel bed, despite its high CPU cost. For such conditions, it is better to use other models for the transport of the bed, i.e., to set the instantaneous velocity of the individual fuel particles. This can be models where the fuel particle velocity is set as a function of the particle size and solid mass fraction in the neighborhood, or it can be empirically based models, where the particle velocities are set based on empirical relations between the type, shape, and size of the fuel (input data) and fuel burnout (simulation data). Development of accurate models of this kind is still one of the major research gaps related to bed models for grate-fired applications.

The combination of the layer model with Lagrangian particle tracking, as presented above, is the most accurate and flexible approach to handle fuel bed models. If faster numerical approaches are required to reduce the CPU cost, more work is still required to identify the framework with the ideal balance between accuracy, reliability, flexibility, and CPU cost, whether it is Lagrangian or Eulerian particle tracking or if it is parallel or serial fuel conversion.

In section 2, the bed model, together with its coupling to the fluid solver, is presented in detail. This also includes a detailed description of how the layer model used in the current approach is implemented. Then, the pilot unit at the University of Stuttgart is presented in section 3, together with some of the main observed features from the experimental campaign. In section 4, the numerical setup is explained before simulation results are compared to experimental results in section 5. Finally, some concluding remarks are made in section 6.

The bed model presented in this paper has been developed to handle various kinds of solid fuels, such as woody biomass or different kinds of wastes. However, for the experiments presented in section 3 as well as for the simulations presented in section 4, only wood chips are considered.

2. NUMERICAL MODEL

As already stated above, the objective of this work is to develop a tool that can be used to simulate grate-fired BtE and WtE plants. There are a large number of commercial, open-source,

https://doi.org/10.1021/acs.energyfuels.1c04204
Energy Fuels 2022, 36, 5852−5867

and in-house CFD solvers available. In the following, we will therefore not discuss the CFD solver in detail but focus on the fuel bed solver. In addition, we will show how we couple the fuel bed solver to the CFD solver. This means that the fluid equations used in the CFD solver will have to be presented.

The heart of a proper fuel bed model is the model that handles the thermochemical conversion of the individual particles in the bed. From now on, we will refer to this model, which is based on the layer model developed at Chalmers,[1,4] as the single-particle model (SPM) (see also the study by Li et al.[15] for more details). The SPM provides a detailed one-dimensional description of the evolution of thermally thick particles that exhibit drying, devolatilization, and char conversion. Given the initial particle properties, the input to the SPM is the surrounding gas and radiative temperatures, together with the mass fraction of oxygen and any gasifying agent in the surroundings. On the basis of this, the SPM calculates the evolution of the particle composition and temperature while yielding the mass flow rate, composition, and temperature of the gaseous products from the particle, which are to be considered as sources to the gas-phase equations.

A fuel bed consists of a large number of particles. As a result of CPU restrictions, a simulation of a full-scale industrial plant cannot handle all of these particles individually. Instead, the SPM is solved for representative particles. This means that each representative particle represents a number of physical particles with the same composition and size. The different representative particles are tracked using the Lagrangian approach and may have different radii and compositions.

We will come back to the velocity of the Lagrangian particles that makes up the bed in section 2.2, while a detailed presentation of the SPM model will be given in section 2.4. Now, we continue by presenting the fluid equations of the CFD solver and show how the source terms from the SPM model enter.

2.1. Fluid Equations. As already mentioned above, the fuel bed (SPM) model itself only handles the evolution of the solid fuel and how it couples to the fluid solver. For the current work, ANSYS Fluent has been chosen as the fluid solver, and the main evolution equations solved by Fluent are presented in eqs 1, 5, 10, 16, and 21. The coupling between Fluent and the bed model is handled through the source terms of the above-mentioned equations. The relevant source terms are presented in eqs 2, 6, 11, 15, and 22. The terms labeled with subscripts SPM, together with $N_{\mathrm{phys},i}$, come directly from the SPM model. In addition to these source terms, also the radiation emitted and absorbed by the particles (eqs 17 and 19) is provided by the SPM model and given as input to Fluent. The coupling between the particle phase and the gas phase is based on the particle centroid method, which is detailed in the work of Zhang et al.[10] All effects of the fuel bed are related to the presence of particles. This means that there is no need to predefine the subvolume containing the fuel bed.

The continuity equation is given by

$$\frac{\partial \alpha\rho}{\partial t} + \nabla(\alpha\rho\boldsymbol{v}) = S_\rho \tag{1}$$

where ρ and $\boldsymbol{v}$ are fluid density and physical velocity, respectively, while

$$S_\rho = \sum_{i=1}^{N_{\mathrm{part,cell}}} S_{\rho,\mathrm{SPM},i} N_{\mathrm{phys},i} \tag{2}$$

is the mass source term as a result of the particles, t is time, and the summation is over all representative particles $N_{\mathrm{part,cell}}$ within the control volume. The mass source term as a result of representative particle i is given by $S_{\rho,\mathrm{SPM},i}$, while $N_{\mathrm{phys},i}$ is the number of physical particles represented by particle i. Expressions for the various source terms as a result of the representative particles ($S_{\rho,\mathrm{SPM},i}$) will be presented in section 2.4.5. The porosity of the fuel bed is given by

$$\alpha = \frac{V_{\mathrm{cell}} - V_{\mathrm{solid}}}{V_{\mathrm{cell}}} \tag{3}$$

where V_{cell} is the volume of a given control volume of the fluid solver,

$$V_{\mathrm{solid}} = \sum_{i=1}^{N_{\mathrm{part,cell}}} \frac{4}{3}\pi r_{\mathrm{p},i}{}^3 N_{\mathrm{phys},i} \tag{4}$$

is the volume occupied by the solid particles within the same control volume, and the radius of particle i is represented by $r_{\mathrm{p},i}$.

The momentum equation is given by

$$\frac{\partial \alpha\rho\boldsymbol{v}}{\partial t} + \nabla(\alpha\rho\boldsymbol{v}\boldsymbol{v}) = -\alpha\nabla P + \nabla(\alpha\tau) + \alpha\rho g + \boldsymbol{F} \tag{5}$$

where P is the fluid pressure, g is the gravitational acceleration, τ is the stress tensor, and $\boldsymbol{F}$ are other external forces, such as, e.g., drag from the particles on the fluid. The particles in the fuel bed have very low velocities, but the relative velocity between the particles and the fluid may still be significant. This yields a pressure gradient over the bed. With all other external forces neglected, we have

$$\boldsymbol{F} = \boldsymbol{S}_{\mathrm{mom,SPM}} \tag{6}$$

where $\boldsymbol{S}_{\mathrm{mom,SPM}}$ is due to the drag exerted from the particles on the fluid (see section 2.4.5).

There are a number of different forms of energy for which the fluid equations can be solved. Here, we have chosen to solve for total energy

$$E = h - P/\rho + v^2/2 \tag{7}$$

where

$$h = \sum_{j=1}^{N_{\mathrm{spec}}} Y_j h_j \tag{8}$$

is the sensible enthalpy, N_{spec} is the number of gaseous species, Y_j is the mass fraction of species j,

$$h_j = \int_{T_{\mathrm{ref}}}^{T} c_{\mathrm{p},j}\,\mathrm{d}T \tag{9}$$

is the sensible enthalpy of species j, and $c_{\mathrm{p},j}$ is its heat capacity. This means that the energy evolution equation is given by

$$\frac{\partial \alpha\rho E}{\partial t} + \nabla(\alpha\boldsymbol{v}(\rho E + P)) = \nabla\left(k_{\mathrm{eff}}\nabla T - \sum h_j \boldsymbol{J}_j + \tau_{\mathrm{eff}}\boldsymbol{v} - q_{\mathrm{r}}\right) + S_{\mathrm{h}} + S_{\mathrm{reac}} + Q_{\mathrm{c}} \tag{10}$$

In the above equation, the source term

https://doi.org/10.1021/acs.energyfuels.1c04204
Energy Fuels 2022, 36, 5852−5867

$$S_h = \sum_{i=1}^{N_{part,cell}} S_{h,SPM,i} N_{phys,i} \tag{11}$$

is due to the hot gas leaving the solid particle and

$$S_{reac} = -\sum \frac{h_j^0 R_j}{M_j} \tag{12}$$

is the source as a result of gas-phase chemical reactions, where h_j^0, M_j, and R_j are the enthalpy of formation, molar mass, and net rate of production, respectively, of species j. Furthermore

$$\boldsymbol{J}_j = -\rho D_{j,m} \nabla Y_j - D_{T_j} \nabla T / T \tag{13}$$

is the diffusive flux of species j, and $D_{j,m}$ and D_{T_j} are its diffusivity and Soret coefficient, respectively. The effective thermal conductivity in the fuel bed is calculated as

$$k_{eff} = \frac{k_{gas} k_{wood}}{X_{wood} k_{gas} + (1 - X_{wood}) k_{wood}} \tag{14}$$

where X_{wood} is the volume fraction of wood (the solid particles) and k_{wood} and k_{gas} are the conductivities of wood and gas, respectively.

The thermal conductivity of the fluid is denoted as k_{eff}, and

$$Q_c = \sum_{i=1}^{N_{part,cell}} Q_{c,SPM,i} N_{phys,i} \tag{15}$$

is the conductive heating of the fluid as a result of the particles.

To account for the effect of radiation, the P1 model is used. This means that the incident radiation G is found by solving

$$\nabla(\Gamma \nabla G) - (\alpha_f + \alpha_p) G + 4\sigma_{SB} \alpha_f T^4 + 4\pi E_p = 0 \tag{16}$$

where

$$E_p = \sum_{i=1}^{N_{part,cell}} \frac{A_{p,i} N_{phys,i} \varepsilon_{p,i} \sigma_{SB} T_{p,i}^4}{\pi V_{cell}} \tag{17}$$

is the radiation emitted by the particles present within the control volume, the surface emissivity of particle i is $\varepsilon_{p,i}$, $A_{p,i} = \pi d_{p,i}^2/4$ is its projected surface area, the radiative diffusivity is given by

$$\Gamma = 1/(3\alpha_{abs}) \tag{18}$$

σ_{SB} is the Stefan−Boltzmann constant, T and T_p are the fluid and particle temperatures, respectively, and $\alpha_{abs} = \alpha_f + \alpha_p$ is the sum of the absorption coefficients as a result of the fluid and particles. The absorption coefficient of the particles is given by

$$\alpha_p = \sum_{i=1}^{N_{part,cell}} \varepsilon_{p,i} A_{p,i} N_{phys,i} / V_{cell} \tag{19}$$

The radiative flux, as represented by q_r in eq 10, can then be found from

$$-\nabla q_r = -4\alpha_f \sigma_{SB} T_f^4 + \alpha_f G \tag{20}$$

The evolution equation of the mass fraction of species j (Y_j) is given by

$$\frac{\partial \alpha \rho Y_j}{\partial t} + \nabla(\alpha Y_j \rho \boldsymbol{v}) = -\nabla \boldsymbol{J}_j + R_j + S_j \tag{21}$$

Here, R_j is the net rate of production of species j as a result of gas-phase reactions, while

$$S_j = \sum_{i=1}^{N_{part,cell}} S_{j,SPM,i} N_{phys,i} \tag{22}$$

is the source term as a result of the particles. Typically, the particles will be a source of water vapor, volatiles, CO, and CO_2 as a result of drying, devolatilization, and char conversion, while they will be a sink of oxygen as a result of char conversion.

2.2. Motion of the Individual Particles in the Bed. When using the Lagrangian approach for particle tracking, it is common to apply a particle collision model to determine the motion of the particles.[2] Such a collision model implies that all particles have to know the position of the other particles in the bed, which is a process that comes at a computational cost that is essentially quadratic in the number of particles. For rigid particles with well-defined shapes, this is an accurate albeit CPU-intensive approach. If the fuel particles are not rigid with well-defined shapes, as is indeed the case for waste fuel, the main effect of using a collision model will be to significantly slow the simulations. For the current approach, we therefore determine the velocity of the fuel particles through an analytical model, which is very fast and requires negligible CPU power. For wastes or other similar fuels, this approach is expected to be at least as accurate as the collision model, while it is much more computationally efficient. In the remainder of this subsection, we will explain the model used to estimate the velocity of the fuel particles.

At the particle inlet, all particles are given an initial velocity $\boldsymbol{v}_{p,bed,in}$. The velocity at various locations along the bed is calculated on the basis of the relative volume change of the particles, such that

$$\boldsymbol{v}_p = \boldsymbol{v}_{p,bed,in} \max[(r_p/r_{p,init})^3, \alpha_v] \tag{23}$$

where r_p and $r_{p,init}$ are the instantaneous and initial particle radii. A lower limit to $\boldsymbol{v}_p$ may be set through the relative velocity fraction α_v. For fuels with very low ash fractions, particles containing only ash may be removed from the simulations to save computational resources. For fuel with a higher fraction of ash, however, the ash may isolate the bed from the grate or shield it from the radiation in the furnace. The ash particles must therefore be retained on the grate until they are transported out to the ash tray.

The vertical velocity of a given particle is modified to make it fall in the direction of gravity if the solid volume fraction of the control volume immediately below the particle is less than a certain critical value, α_c. The effect of this is that new particles will fall into the control volume that had a low solid volume fraction, such that its volume fraction is increased above α_c, and the bed compression will thereby stop.

2.3. Inert Particles. Some particles will be inert even under the high heat flux experienced in a grate-fired furnace. This is the case for, e.g., metal particles. Here, we assume that inert particles have high conductivities, which is indeed the case for metal particles, and hence, we will use a thermally thin approximation to describe them (a particle is considered as thermally thin if its size and conductivity are such that, for the given heating rate, the temperature gradients inside the particle are negligible). For inert particles, we only have to solve the temperature equation, which is given by

https://doi.org/10.1021/acs.energyfuels.1c04204
Energy Fuels 2022, 36, 5852−5867

$$\frac{dT_p}{dt} = \frac{A_p}{m_p c_{p,p}}[h(T_g - T_p) + \varepsilon\sigma({T_{rad}}^4 - {T_p}^4)] \quad (24)$$

for thermally thin particles. The mass, density, and radius of an inert particle are kept constant for all times.

2.4. Reactive Particles. As already stated above, the physical particles in the bed are lumped together into representative particles. The evolution of each representative particle is then tracked using the SPM. In this subsection, we will present the SPM in more detail. In the SPM model, an account is made for the reactive fuel particles to be thermally thick. This means that the particle interior must be resolved. In the current implementation, this is performed by use of the so-called layer model, where the particles are assumed to be spherically symmetric, such that the evolution of the various layers of fuel can be tracked in a one-dimensional (1D) fashion. The particle is divided into four layers: (1) wet fuel, (2) dry fuel, (3) char, and (4) ash. These four layers are associated with four thin boundaries where the following processes occur: (I) drying, (II) devolatilization, (III) char conversion, and (IV) heat and mass exchange between the particle and fluid (external boundary). A graphical representation of the four layers and boundaries is given in Figure 1. In

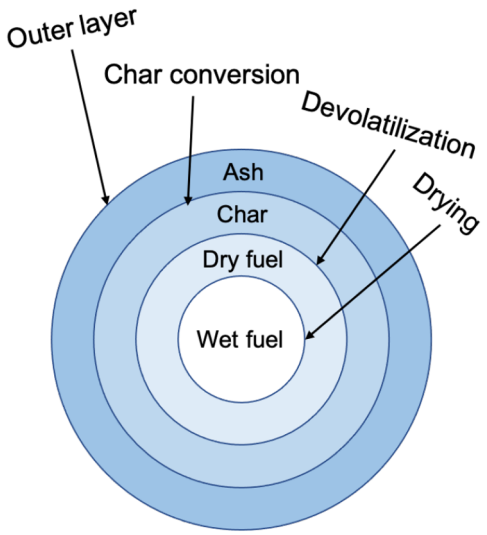

Figure 1. Layers and boundaries for a reactive particle.

the following, subscripts b,i represent the drying (i = 0), devolatilization (i = 1), char conversion (i = 2), and external (i = 3) boundaries. In the same way, subscripts p,i represent the wet fuel (i = 0), dry fuel (i = 1), char (i = 2), and ash (i = 3) layers. The radius of the drying boundary is therefore given by $r_{b,0}$, while the radii of devolatilization, char conversion, and external surface are given by $r_{b,1}$, $r_{b,2}$, and $r_{b,3}$, respectively. The corresponding layer volumes are given by

$$V_{p,i} = \frac{4}{3}\pi {r_{b,i}}^3, \quad \text{for } i = 0$$

$$V_{p,i} = \frac{4}{3}\pi({r_{b,i}}^3 - {r_{b,i-1}}^3), \quad \text{for } i > 0 \quad (25)$$

On the basis of this, the mass of the different layers becomes

$$m_{p,i} = V_{p,i}\rho_{p,i} \quad (26)$$

where $\rho_{p,i}$ is the material density of layer i. The total mass of the particle is therefore given as

$$m_{p,tot} = \sum_{i=0}^{3} m_{p,i} \quad (27)$$

When the particles enter the simulation, they consist primarily of wet fuel, but for numerical reasons, they are also initialized with very thin layers of dry fuel, char, and ash, with a relative radial extent of p_{dry}, p_{char}, and p_{ash}, respectively. This means that the boundaries for drying, devolatilization, and char conversion are initially located at

$$r_{b,0} = R_p(1 - p_{dry} - p_{char} - p_{ash}) \quad (28)$$

$$r_{b,1} = R_p(1 - p_{char} - p_{ash}) \quad (29)$$

$$r_{b,2} = R_p(1 - p_{ash}) \quad (30)$$

$$r_{b,3} = R_p \quad (31)$$

where R_p is the radius of the particle. The initial temperature of the particle is set equal for all layers.

2.4.1. Time Evolution of the SPM Model. We will now continue by describing how we solve for the evolution of the different layers and boundaries of the representative particles. The variables to solve are the temperature of the different layers ($T_{p,i}$) and boundaries ($T_{b,i}$), in addition to the radii of the boundaries ($r_{b,i}$) and the mass of the layers ($m_{p,i}$).

The radii of the center of each layer [note that this is different from the radius of the boundaries ($r_{b,i}$)] is determined by

$$r_{p,i} = \left(\frac{{r_{b,i-1}}^3 + {r_{b,i}}^3}{2}\right)^{1/3} \quad (32)$$

Now, the solution for the next time step is determined through an iterative process, where the change in the mass of the layers is found from

$$\frac{dm_{p,0}}{dt} = -R_{b,0}/Y_{water} \quad (33)$$

$$\frac{dm_{p,1}}{dt} = R_{b,0}/Y_{water,db} - R_{b,1}/Y_{dry,db} \quad (34)$$

$$\frac{dm_{p,2}}{dt} = R_{b,1}Y_{ash,db}/Y_{dry,db} + R_{b,1\_to\_char} - R_{b,2} \quad (35)$$

$$\frac{dm_{p,3}}{dt} = m_{aic}R_{b,2}/m_{p,2} \quad (36)$$

where Y_{water} and $Y_{water,db} = Y_{water}/(1 - Y_{water})$ are the mass fractions of moisture in the wet fuel on a raw and dry basis, respectively. Here, and in the following, subscript "db" refers to "dry basis". The reaction rates, $R_{b,i}$, are the rate of consumption at boundary i in units of kg/s. For example, $R_{b,1}$ is the total mass loss from the devolatilization zone, accounting for all of the mass that is converted to light gases, tars, and char. To keep track of the mass in the char layer, we also need to know $R_{b,1,char}$, which is the part of $R_{b,1}$ that goes to char. Furthermore, $Y_{ash,db}$ is the mass fraction of ash, while $Y_{dry,db} = 1 - Y_{ash,db}$ is the mass fraction of dry fuel. The change in the amount of ash in the char layer is given by

https://doi.org/10.1021/acs.energyfuels.1c04204
Energy Fuels 2022, 36, 5852−5867

$$\frac{dm_{aic}}{dt} = R_{b,1}Y_{ash,db}/Y_{dry,db} - \frac{dm_{p,3}}{dt} \quad (37)$$

The temperature of the external boundary of the particle is calculated on the basis of the thermal energy that is transported to and from the surface. We therefore employ the energy balance at the external surface of the particle, which is given by

$$h(T - T_{surf}) + \varepsilon\sigma({T_{rad}}^4 - {T_{surf}}^4) - k_{ash}\left.\frac{dT}{dr}\right|_{surf,ash} = 0 \quad (38)$$

where T_{rad} is the radiative temperature of the particle surroundings, T_{surf} is the surface temperature of the particle, while k_{ash} is the conductivity of the ash. Finally, $\left.\frac{dT}{dr}\right|_{surf,ash}$ is the temperature gradient over the ash layer. In the above equation

$$h = \frac{NuD_{th}}{d_p} \quad (39)$$

is the conductive heat transfer coefficient when $D_{th} = k_{eff}/c_p\rho$ is the thermal diffusivity of the fluid and c_p is its heat capacity. To calculate the heat transfer coefficient, we assume that the Nusselt number is equal to the Sherwood number. The Sherwood number, where an account is made for the effect of porosity (α), is found through the correlation of Gunn[16]

$$Sh_0 = (7 - 10\alpha + 5\alpha^2)(1 + 0.7{Re_p}^{0.2}Pr^{1/3}) + (1.33 - 2.4\alpha + 1.2\alpha^2){Re_p}^{0.7}Pr^{1/3} \quad (40)$$

where the Prandtl number of the fluid is denoted as Pr, while $Re_p = u_{rel}d_p/\nu$ is the particle Reynolds number as a result of the relative velocity difference, u_{rel}, between the particle and fluid, and ν is the kinematic viscosity. The gaseous outflow from the particles as a result of the net molar production of gas coming from devolatilization, drying, and char conversion is typically referred to as the Stefan flow. The effect of the Stefan flow is to reduce the net heat and mass transport to the particle. This is accounted for by multiplying the Sherwood number for non-reactive particles, as given in eq 40, with the following corrective term:

$$\beta = \frac{\phi}{\exp\phi - 1} \quad (41)$$

where $\phi = \dot{n}_{total}/k_{im}$. The total molar production rate is given by

$$\dot{n}_{total} = \sum_{i=1}^{N_{spec}} \dot{n}_i \quad (42)$$

where $\dot{n}_i$ is the molar production rate of species i, the number of species involved in the surface reactions is N_{spec}, and the mass transfer coefficient is given by

$$k_{im} = \frac{C_g D_g Sh_0}{D_p} \quad (43)$$

Here, C_g is the molar concentration of gas in the boundary layer, and D_g is species diffusivity. The resulting Sherwood number, including effects of both the porosity of the bed and the Stefan flow, is therefore given by

$$Sh = Sh_0\beta \quad (44)$$

As already stated above, the Nusselt number is assumed to be equal to the Sherwood number, such that $Nu = Sh$.

The temperature of the inner boundaries is calculated on the basis of the temperature of the neighboring layers, in addition to the heat release rate at the boundary itself. The general way for calculating the temperature of the inner boundaries can be found in the Temperature of Inner Boundaries section of the Appendix.

2.4.2. Char Conversion Boundary. The char fraction of a solid fuel can be oxidized by oxygen or gasified by steam or carbon dioxide. For an air-fired WtE or BtE furnace based on the grate technology, essentially all of the char is converted through reactions with oxygen. For the current work, we do not therefore account for gasification of char.

When char is oxidized by oxygen, both CO and CO_2 may be produced, and the resulting reaction becomes $\omega_c C + O_2 \rightarrow (\omega_c - 1)CO + (2 - \omega_c)CO_2$. The net stoichiometric factor of the oxidation reaction is given by[17]

$$\omega_c = \frac{2(1 + 4.3\exp(-3390/T_{b,2}))}{2 + 4.3\exp(-3390/T_{b,2})} \quad (45)$$

If $\omega_c = 1$, only CO_2 is produced, while only CO is produced in the limit of $\omega_c = 2$. From Figure 2, we see that the value of the stoichiometric factor varies between 1 and 1.4 for the temperatures of interest for char oxidation.

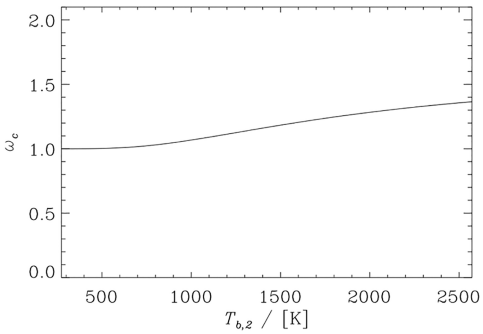

Figure 2. Net stoichiometric factor, ω_c, as a function of the temperature of the char conversion boundary (see eq 45).

The char conversion rate as a result of oxidation is found from

$$R_{b,2} = M_C\omega_c C_{O_2}\frac{\beta_r\beta_d}{\beta_r + \beta_d}A_{b,2} \quad (46)$$

where $A_{b,2}$ is the area of the char conversion boundary,

$$\beta_r = A_r T_{b,2}\exp(-E_r/(RT)) \quad (47)$$

is the kinetic rate of the char conversion reaction,

$$\beta_d = \frac{h_{mi}h_{mia}}{h_{mi} + h_{mia}} \quad (48)$$

is the diffusion rate of oxygen to the particle surface, and $T_{b,2}$ is the temperature of the char conversion boundary. An account is made for the diffusion of oxygen both through the boundary layer (h_{mi}) and the ash layer (h_{mia}). The first term accounts for diffusion through the boundary layer

https://doi.org/10.1021/acs.energyfuels.1c04204
Energy Fuels 2022, 36, 5852−5867

$$h_{mi} = ShD_g/d_p \tag{49}$$

where the Sherwood number is found from eq 44, while the second term handles diffusion through the ash layer

$$h_{mia} = \frac{D_g {\alpha_{ash}}^2}{r_{b,3} - r_{b,2}} \tag{50}$$

where α_{ash} is the porosity of the ash layer.

Using the above equations, the production rates of the gas-phase species as a result of char conversion can now be found through the following expressions:

$$\dot{W}_{char,CO_2} = R_{b,2}\frac{M_{CO_2}}{M_C}\left(\frac{2-\omega_c}{\omega_c}\right) \tag{51}$$

$$\dot{W}_{char,CO} = 2R_{b,2}\frac{M_{CO}}{M_C}\left(\frac{\omega_c - 1}{\omega_c}\right) \tag{52}$$

$$\dot{W}_{char,O_2} = -\dot{W}_{char,CO_2}\frac{M_{O_2}}{M_{CO_2}} - \frac{1}{2}\dot{W}_{char,CO}\frac{M_{O_2}}{M_{CO}} \tag{53}$$

where the molar mass of species i is denoted as M_i. Finally, the heat of reaction for char conversion is given by

$$Q_{b,2} = \frac{R_{b,2}}{M_C}\left(2M_{CO}L_{CO}\frac{\omega_c - 1}{\omega_c} + M_{CO_2}L_{CO_2}\frac{2-\omega_c}{\omega_c} - L_C M_C\right) \tag{54}$$

where L_i is the enthalpy of formation of species i.

2.4.3. Devolatilization Boundary. Because volatile gases go off at an interval of temperatures, we split the dry fuel layer in N_{sub} equidistant sublayers. The total mass sink of the devolatilization layer is then given by the sum of the mass loss from all sublayers

$$\dot{m}_{dry,lay} = \sum_{j=0}^{N_{sub}-1} \dot{m}_d(r_{sub,j})/Y_{dry,db} \tag{55}$$

where $r_{sub,j}$ is the radius of the center of sublayer j and

$$\dot{m}_d = -\dot{m}_{sub,gas} - \dot{m}_{sub,tar} - \dot{m}_{sub,char} \tag{56}$$

In the work presented here, three competitive reactions are used to represent devolatilization. The production rates of non-condensable gas, tars, and char are therefore given by

$$\begin{aligned} \dot{m}_{sub,gas} &= k_1 m_{sub,j} Y_{dry,db} \\ \dot{m}_{sub,tar} &= k_2 m_{sub,j} Y_{dry,db} \\ \dot{m}_{sub,char} &= k_3 m_{sub,j} Y_{dry,db} \end{aligned} \tag{57}$$

respectively. Note that, because dry fuel also contains ash, eq 55 contains a $1/Y_{dry,db}$ term that ensures that all four components (gas, tar, char, and ash) are indeed removed from the dry fuel layer. The Arrhenius expression for the different competitive devolatilization reactions is

$$k_i = A_i \exp\left(\frac{-E_i}{RT}\right) \tag{58}$$

and $m_{sub,j}$ and $T_{sub,j}$ are the mass and temperature of sublayer j, respectively.

From the total mass sink of the dry fuel layer, as given in eq 55, the reaction rate of devolatilization used in eqs 34 and 35 is given as

$$R_{b,1} = \dot{m}_{dry,lay} Y_{dry,db} \tag{59}$$

where $R_{b,1}$ represents the rate of which dry fuel is converted to gas, tar, or char (i.e., the ash part is excluded from this term).

The corresponding source in the char layer is found from

$$\dot{m}_{char,lay} = \sum_{j=0}^{N_{sub}-1} \dot{m}_c(r_{sub,j}) \tag{60}$$

where

$$\dot{m}_c = \dot{m}_{sub,char} + \frac{Y_{ash,db}}{Y_{dry,db}}\dot{m}_d \tag{61}$$

The last term in this equation comes from the fact that the dry fuel contains some ash. Here, we assume that this ash remains within the particle after the volatiles have gone off, which means that it contributes to the mass of the char layer. This is not entirely correct for biomass or waste feedstocks with a high content of inorganic (ash) elements that can be released to the gas phase during devolatilization. For such fuels, ash-forming elements are also released in significant amounts during the devolatilization stage. From this, we find that the production rate, as used in eq 35, is given by

$$R_{b,1,char} = \dot{m}_{char,lay} - R_{b,1}\frac{Y_{ash,db}}{Y_{dry,db}} = \sum_{j=0}^{N_{sub}-1} \dot{m}_{sub,char} \tag{62}$$

From the change in solid mass of the dry fuel layer that we have calculated above, we will now continue by obtaining the corresponding release rates of gas-phase species as a result of devolatilization. The release rates of non-condensable gases and tars are given by

$$\dot{W}_{gas} = \sum_{j=0}^{N_{sub}-1} \dot{m}_{sub,gas} \tag{63}$$

and

$$\dot{W}_{tar} = \sum_{j=0}^{N_{sub}-1} \dot{m}_{sub,tar} \tag{64}$$

respectively. For a given fuel, we assume the composition of tars ($Y_{tar,i}$) and non-condensable gases ($Y_{gas,i}$) to be constant in time. The volatile release rate of species i then becomes

$$\dot{W}_{devol,gas,i} = \dot{W}_{gas} Y_{gas,i} \tag{65}$$

and

$$\dot{W}_{devol,tar,i} = \dot{W}_{tar} Y_{tar,i} \tag{66}$$

The heat of reaction for devolatilization is set to $Q_{b,1} = 0$.

2.4.4. Drying Boundary. Heat that is transported to the drying boundary of the particle will be used to either heat the wet fuel or evaporate water from the drying boundary. Several models exist that calculate the evaporation rate of water.[18] The three most common ones are (1) the kinetic model, (2) the thermal model, and (3) the equilibrium model. In this work, we make use of a smoothed version of the thermal drying model, where the fraction of heat that is used to evaporate water is given by[4]

https://doi.org/10.1021/acs.energyfuels.1c04204
Energy Fuels 2022, 36, 5852−5867

$$F_{b0} = \min(1.0, f_{b0}) \tag{67}$$

where

$$f_{b0} = \frac{10^{8.07131 - 1730.63/(T_{b,0} - 39.724)}}{760} \tag{68}$$

The remaining fraction is used to heat the interior of the particle. See Figure 3 for a representation of F_{b0} as a function of the temperature.

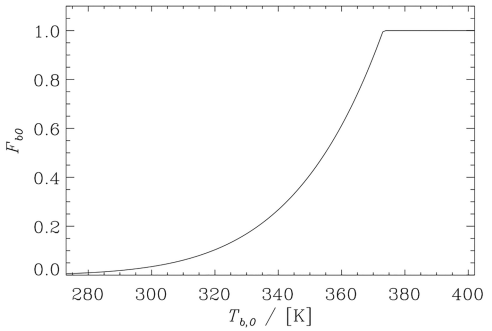

Figure 3. Fraction of heat used to evaporate water, F_{b0}, as a function of the temperature of the evaporation boundary.

On the basis of the above, the total amount of heat that is used to evaporate water at the boundary is given by

$$Q_{b,0} = k_{p,1} A_{b,0} \left.\frac{dT}{dr}\right|_{b0,p1} F_{b0} \tag{69}$$

The temperature at the boundary can now be found through eq 81. An alternative way of finding the temperature of the drying boundary based on the same assumptions is presented in the Temperature of the Drying Boundary section of the Appendix.

With the knowledge of $Q_{b,0}$, the reaction rate of the drying layer is given by

$$R_{b,0} = Q_{b,0}/L_{water} \tag{70}$$

where $L_{water} = 2.26 \times 10^6$ J/kg is the latent heat of water. The release rate of steam to the gaseous surrounding is therefore given simply by

$$\dot{W}_{drying,H_2O} = R_{b,0} \tag{71}$$

2.4.5. Source Terms for the Gas-Phase Equations. All four boundaries discussed in the previous subsections contribute in some way or other with sources in the fluid equations. In the following, we will describe these source terms as a result of the presence of individual physical particles belonging to representative particle *i*.

The species source term in the gas-phase equation, as introduced in eq 22, is the sum of the contributions from all three internal boundaries.

$$S_{j,SPM} = \dot{W}_{drying,j} + \dot{W}_{devol,gas,j} + \dot{W}_{devol,tar,j} + \dot{W}_{char,j} \tag{72}$$

From this, the source term of the gaseous continuity equation, as used in eq 2, is found as

$$S_{\rho,SPM} = \sum_{j=1}^{N_{spec}} S_{j,SPM} \tag{73}$$

From eq 72, we can also find the source term for the energy equation by multiplying the species source term with the enthalpy of that species, evaluated at the surface temperature of the particle, and summing over all species

$$S_{h,SPM} = \sum_{j=1}^{N_{spec}} S_{j,SPM} h_j \tag{74}$$

where h_j is the enthalpy of species *j*. With the value of the heat transfer coefficient given by eq 39, the total heat loss of the particle as a result of convective transport from the fluid is found as

$$Q_{c,SPM} = -hA_p(T - T_p) \tag{75}$$

Finally, the source term in the momentum equation as a result of the presence of the particle fuel bed (eq 6) is given by the Darcy–Forchheimer expression

$$\boldsymbol{S}_{mom,SPM} = -\left(\frac{\mu}{K}\boldsymbol{v} + \frac{1}{2}C_2\rho|\boldsymbol{v}|\boldsymbol{v}\right) \tag{76}$$

where $\mu = \rho\nu$ is dynamic viscosity,

$$K = \frac{\tilde{d}_p^{\,2}}{150}\left(\frac{\alpha^3}{(1-\alpha)^2}\right) \tag{77}$$

is the permeability of the bed, $\tilde{d}_p$ is the mean particle diameter, and

$$C_2 = \frac{3.5}{\tilde{d}_p}\frac{(1-\alpha)}{\alpha^3} \tag{78}$$

is the inertial resistance factor.

3. EXPERIMENTAL SECTION

The bed model and its coupling to the CFD model is presented in the above sections. A comparison of results from simulations to the new model will now be performed against pilot-scale experiments performed at the University of Stuttgart (USTUTT). The pilot rig at USTUTT is a 240 kW_{th} forward moving grate incinerator, which for the experiment of interest is fired with wood chips at a rate of 43.9 kg/h. This yields a thermal power of 208 kW_{th}. More details about the fuel (wood chips) used in this experiment can be found in Tables 1 and 2. A schematic view of the facility is shown in Figure 4. The pilot primary chamber is 0.5 m wide and 0.53 m high. The length of the grate is 1.14 m, while the length of the primary chamber at the level of the grate is 1.34 m.

Table 1. Details about the Wood Chips Used as Fuel

	amount	unit
moisture	7.53	%
volatile (db)	81.0	%
ash (db)	0.45	%
fixed C (calculated, db)	18.55	%
LHV (db)	18639	kJ/kg

For the current test, the total mass flow rate of air is 294 kg/h, corresponding to a total air excess ratio of 1.4 with the given input rate of wood chips. Furthermore, 40% of the air is provided through the primary inlets, while 60% comes through the three secondary inlets. The primary air is distributed such that $^2/_3$ comes from the first primary air inlet, while the rest comes from the second. The distribution of air flow between the three secondary air inlets is 44/39/17% on inlet 1/2/3, respectively.

https://doi.org/10.1021/acs.energyfuels.1c04204
Energy Fuels 2022, 36, 5852−5867

Table 2. Details about Particle Size Distribution of the Wood Chips Used as Fuel

sieve size (mm)	retained percentage of coarse wood chips (%)
>20	11.33
>10−20	48.68
>7.1−10	15.75
>4.0−7.1	18.80
>1.18−4.0	4.69
<1.18	0.73

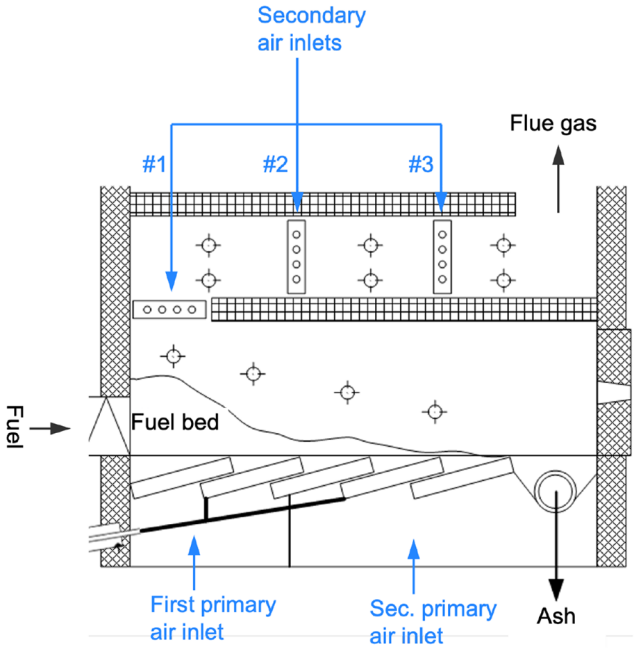

Figure 4. Schematic view of the pilot rig at the University of Stuttgart.

The average velocity of the fuel particles at the beginning of the bed is not easily measured. Instead, it is estimated on the basis of the movement of the grate elements to be 1.6 mm/s. This is, however, an upper estimate and likely to yield somewhat too low of a residence time in the bed. For the experiments, the total heat loss through the furnace walls is found to be 12 kW, which corresponds to roughly 6% of the total power for the current test. The heat flux through the walls is then estimated by assuming that the flux is the same for all external walls.

The grate consists of cast iron elements with an organization in the $x-y$ plane, as seen in Figure 4. In the z direction, there are a total of seven grate elements laying side by side. The primary air enters through the gaps between these elements.

It is known that a fuel bed can be ignited from either the top, by the radiative load from the flame and hot walls in the combustion chamber, or the bottom, as a result of a hot grate and primary air.[19] In Figure 5, we show the measured temperature of the grate elements (circles) and in the bed 4 cm above the grate (triangles) as a function of the downstream distance along the grate. Close to the fuel inlet (leftmost points), we see that the grate has a higher temperature than the bed. This is indeed indicative of the bed being ignited from below. This may be surprising because the primary air that enters the wind box is close to room temperature. However, the reason that the ignition is from below is that the grate is heated both through radiative and conductive heating from any hot part of the bed just above the grate surface and, more importantly, through conduction of heat in the upstream direction along the cast iron grate elements. When the downstream part of the grate is heated by local char conversion, this heat is conducted upward. Because the primary air has to pass through the narrow gaps between the grate elements, the

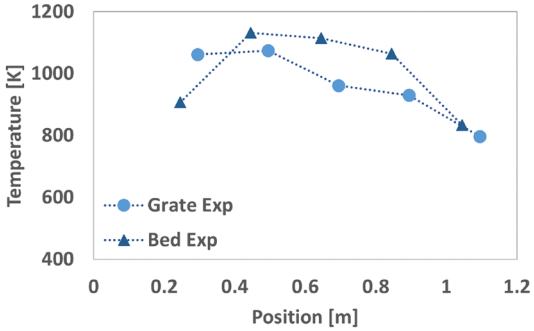

Figure 5. Temperatures measured on the grate and in the bed of the pilot rig at the University of Stuttgart.

hot grate will heat the primary air such that, when it enters the bed, it will quickly devolatilize the fuel and eventually start to convert char. This process makes the char conversion move further and further upstream along the bed. The result of this is that, already relatively close to the fuel inlet, the hot grate will feed hot air to the first layer of particles in the bed. These particles already have a significant char layer as a result of fast devolatilization even further upstream on the grate, which will now be oxidized to produce hot flue gas. This hot gas will be convected upward in the bed while being cooled by the colder bed particles further up. This explains why the grate elements are warmer than the thermocouple placed in the bed (4 cm above the grate) at the position of the first (leftmost) temperature measurement. As we move further downstream along the grate, char conversion occurs also higher up in the bed, and the bed temperature will then be higher than the temperature of the grate. One of the main conclusions that can be drawn from the discussion above is that the thermal properties of the grate may determine how the bed is ignited (from above or below), which has a significant effect on the bed behavior.

4. SIMULATIONS

ANSYS Fluent is used as the CFD solver for all simulations presented in this work, and the user defined function (UDF) framework of Fluent is used to couple the bed model with the CFD solver. A two-dimensional mesh that consists of 2.5×10^3 control volumes is generated. The average values for the aspect ratio, skewness, and orthogonal quality are 1.1, 0.02, and 0.997, respectively. The solver is run in transient mode, while the basic version of Fluent's Lagrangian particle solver is used to keep track of the representative particles of the fuel bed. Fluent's own machinery for particle energy and conversion is, however, turned off. This is all handled through the UDFs.

To represent the chemical reactions in the gas phase, the two-step mechanism of Westbrook and Dryer[20] was chosen as a result of its popularity within the industry and its low computational costs. This mechanism consist of two steps, where the first step oxidizes methane to carbon monoxide and steam, while the second step oxidizes carbon monoxide to carbon dioxide.

$$CH_4 + 3/2O_2 \rightarrow CO + 2H_2O \quad \text{(R1)}$$

$$CO + 1/2O_2 \rightarrow CO_2 \quad \text{(R2)}$$

The fuel used in the experiment is wood chips. Because the SPM model can only represent simplified spherical or cylindrical geometries, it is not possible to exactly represent wood chips. In the simulations, individual fuel particles are therefore represented as spherical objects.

At the devolatilization boundary, dry wood devolatilizes following three competitive reactions, producing light gases, tars, and char. The Arrhenius parameters for the three

https://doi.org/10.1021/acs.energyfuels.1c04204
Energy Fuels 2022, 36, 5852−5867

reactions are given in Table 3, which, by use of eqs 57 and 58, yields the production rate of light gases, tars, and char. With this devolatilization model, an account is made for the fact that both light gases and tars leave the wood particles as a gaseous phase. As a result of the simplified gas-phase reaction model used, there is no tar in the reaction kinetics. For this study, the composition of the tar is therefore set equal to the composition of light gases, such that they both consist of 42% CO, 12% CO_2, 30% H_2O, and 16% CH_4, on a mass basis. For char oxidation, the Arrhenius parameters of Thunman et al.[1] (A_r = 1.715 m/K/s, and $E_r = 7.48 \times 10^4$ J/mol) are used in eq 47 to calculate the char conversion kinetics.

Table 3. Arrhenius Parameters for the Three Competitive Devolatilization Reactions of Dry Wood[1]

i	reaction	A_i (s^{-1})	E_i (J/mol)
1	dry wood → light gases	13.0×10^7	1.40×10^5
2	dry wood → tars	20.0×10^7	1.33×10^5
3	dry wood → char	1.08×10^7	1.21×10^5

The two-dimensional geometry used for the simulation of the pilot rig of USTUTT is shown in Figure 6. The green mesh represents the porous grate. The solid fuel enters through a 20 cm high opening just above the grate on the left-hand side. The black external walls are associated with a heat flux of 6 kW/m^2, corresponding to a total heat loss of 12 kW for the entire pilot, as was found from the experiments. The wall between the primary and secondary chambers is simulated as a coupled brick wall. As such, a significant fraction of the heat liberated in the secondary combustion chamber is conducted to the ceiling of the primary combustion chamber. This results in a hot surface that radiates down on the upper part of the fuel bed.

The grate elements in the experiment consist of cast iron, which means that heat is easily transported through the grate elements opposite the flow direction of the bed. As discussed in the previous subsection, this facilitates ignition of the bed from below. Because cast iron has a significant absorption coefficient, the radiative heat from the bed immediately above the grate will also heat the grate itself and, through that, the primary air that passes through the grate elements on its way to the bed. In the simulations, however, the grate is emulated as a porous zone, which does not interact with radiation. On top of this, to reduce thermal inertia and, hence, to reduce the required run time to reach the stationary state, the porosity of the grate is chosen to be very high, which yields too low thermal conductivity. To compensate for this shortcoming, the temperature of the primary air is set to 1073 K for the first wind box and 700 K for the second wind box. This is, however, not an accurate representation because the temperature of the primary air as it leaves the grate will depend upon the exact condition of the bed above and the position on the grate. As such, the grate temperature is not expected to be accurately predicted in the current simulation. To be able to make better predictions of the grate temperature, one would have to resolve the bed also in the third direction, such that the grate elements and the gaps between them can be properly simulated, which demands a three-dimensional mesh. Because the aim of this work is just to do a first comparison of results obtained with the new model against experimental results, it is beyond the

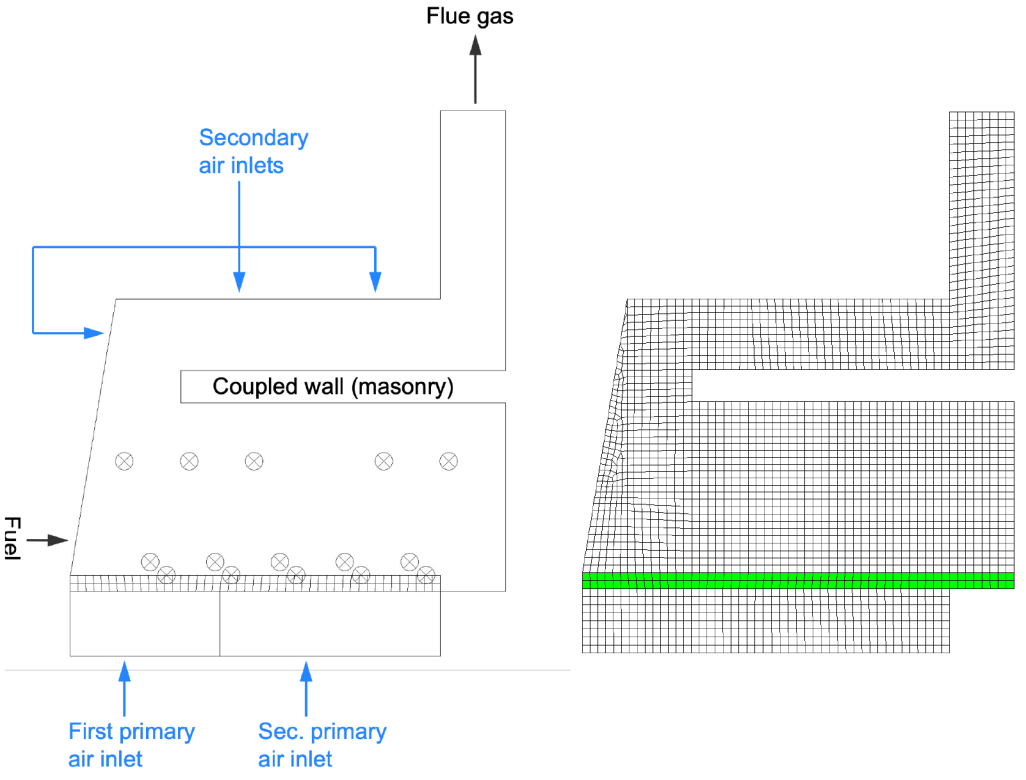

Figure 6. Schematic view of the numerical geometry (left) and mesh used for the main simulations (right). The upper row of circles in the left panel corresponds to the temperature measurement ports in the primary chamber, and the middle row (which is just 4 cm above the grate) represents the positions of the measurement ports in the fuel bed, while the lower row gives the positions of the measurement ports in the grate.

https://doi.org/10.1021/acs.energyfuels.1c04204
Energy Fuels 2022, 36, 5852−5867

scope of this work to perform such three-dimensional simulations.

5. RESULTS

In this section, results from the six simulation cases listed in Table 4 will be presented and compared to results from the experiments described in section 3. Case B in Table 4 is defined as our base case. The experimental results that we compare against are relatively well-defined, but they do still contain a few unknowns. In particular, the bed velocity and the size of the fuel particles are not accurately known. More specifically, because the fuel consists of wood chips, the fuel particle size is not well-defined and will have a certain distribution. Indeed, the particle size distribution for the wood chips used in the experiments shows that 75% of the particles have sizes between 0.5 and 2 cm. Simulations with three different particle sizes, denoted B−, B, and B+ in Table 4, and three different bed velocities, denoted A, B, and C, are therefore performed to investigate the sensitivity of the results on these unknowns. In addition, we also show results from a simulation with a lower fuel feeding rate (BM−). The number of Lagrangian particle parcels (representative particles) in the domain at any given time during the steady state is between 10^3 (case B−) and 4×10^3 (case B+). The physical particles, representing wood chips, consist of 7% moisture and 0.4% ash (as received) and, for the base case, have a diameter of 1 cm.

Table 4. Summary of the Six Different Cases

case	d_p (cm)	$v_{p,bed,in}$ (mm/s)	$\dot{m}_{fuel}$ (kg/h)
A	1.0	1.6	43.9
B−	0.5	0.8	43.9
B	1.0	0.8	43.9
B+	2.0	0.8	43.9
C	1.0	0.4	43.9
BM−	1.0	0.8	30.0

As discussed in the previous sections, the numerical handling of the grate itself may be controlling the ignition process of the bed. Because it is not possible to handle the grate and the openings for the primary air appropriately in two dimensions, a simplified grate handling is adopted in this work. Because of this, the temperature of the primary air, which is set to 1073 and 700 K for the two wind boxes, is used to partly compensate for this shortcoming. From Figure 7, we see that the simulated temperature on the grate varies with both the particle size and initial inlet particle velocity. In general, we see that small particles and low inlet particle velocities yield higher temperatures on the first part of the grate and lower temperatures on the last part of the grate, while the opposite is true for high particle inlet velocities. Interestingly, large particles yield relatively low temperatures over the entire grate. This is due to an overall lower mass transfer coefficient and, hence, lower char conversion for the largest particles. We will come back to the reason for the various temperature evolution later, but now, we conclude the discussion of the grate temperatures by noticing that the experimental measurements (dashed black line) are essentially found between the extremes of the numerical results. This indicate that the difference between the experimental and numerical results may be due to the aforementioned unknowns. Some other reasons for the differences may be that the experimental measurements are performed slightly inside the front side of the cast iron elements, while the numerical results are from the surface of the porous representation of the grate. Also, of course, the rough approach used to compensate for the simplified grate handling may introduce errors, for example, as a result of the fact that only two different inlet temperatures are used.

5.1. Variable Fuel Particle Size.

We continue by investigating the effect of the initial size of the fuel particles in more detail. In Figure 8, the particles in the bed are color-

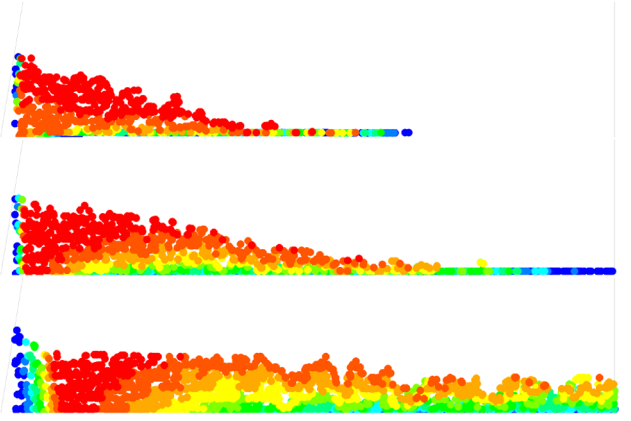

Figure 8. Particles in the fuel bed, color coded by mass of char, for cases (top) B−, (middle) B, and (bottom) B+. The color coding corresponds to the following fraction of the maximum mass of char: dark blue, <10%; green, ∼50%; and dark red, >90%.

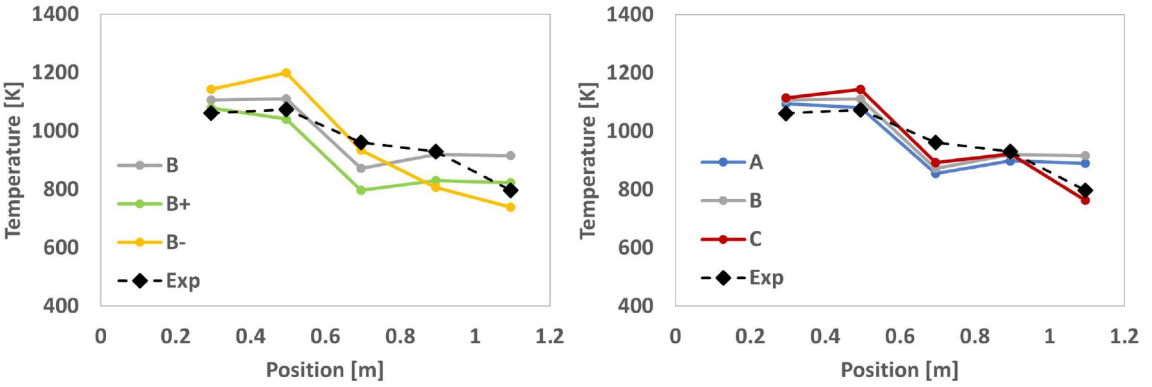

Figure 7. Temperature along the grate for (left) cases B−, B, and B+ and (right) cases A, B, and C.

https://doi.org/10.1021/acs.energyfuels.1c04204
Energy Fuels 2022, 36, 5852−5867

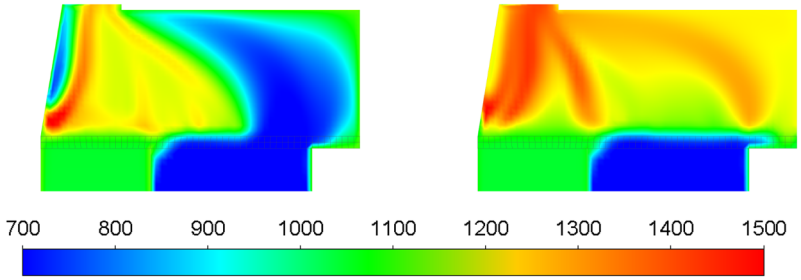

Figure 9. Contours of fluid temperature for (left) B− and (right) B.

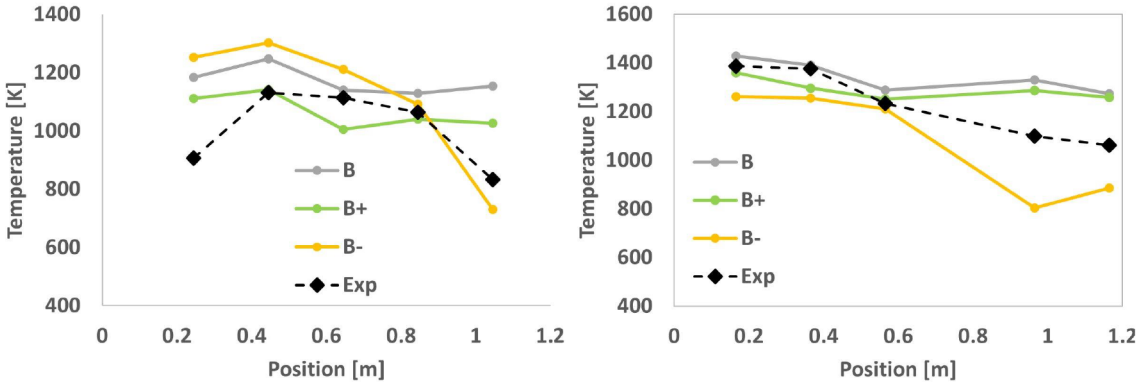

Figure 10. Temperature (left) along the fuel bed and (right) in the primary combustion chamber.

coded by the amount of char in the particle (red is high, and blue is low). By inspection of the particles just after they enter the bed (left side), we see that the larger the particles, the longer it takes for the particles to completely devolatilize to char, i.e., for the color in the figure to change from blue to red. This is because the devolatilization is a heat-limited process, and the heat transfer coefficient scales as one over the particle diameter, in analogy to the mass transfer coefficient as given by eq 49. We also observe that the limiting process for fuel burnout is the char conversion process. For the smallest particles (upper panel), the conversion is fast and full burnout is accomplished well before the end of the grate. For the intermediately sized particles, all of the char is essentially converted at the end of the bed, while for the largest particles, full conversion is far from achieved. The reason for this can be understood from eq 49, which shows that the mass transfer coefficient through the particle boundary layer is inversely proportional to the particle size (in analogy with the heat transfer coefficient discussed previously). The smallest particles are therefore able to consume more of oxygen from the primary air that passes by them.

In comparison of the integrated net mass release from the bed model to the mass flow rate of the fuel feed, the percentage of the fuel that is converted in the simulations is 99.6% for the base case (B), which is in accordance with the observation that essentially all of the fuel is converted before the end of the grate. For the case with larger particles (case B+), however, this percentage is significantly lower (91.6%), which is in qualitative agreement with the fact that not all of the fuel particles are converted at the fuel bed outlet.

We now proceed to validate the elemental balance of the simulations. The elemental input rate is found by considering the proximate analysis, as presented in Table 1, together with the composition of the volatiles (see section 4) and the fuel feeding rate, as given in Table 4, while the elemental output rate is obtained by integrating the mass flux of each element over the simulation outlet. By comparison of the two, we find that, for the base case (case B), the elemental output rate of carbon is 6 wt % lower than the input rate, while for hydrogen and oxygen, it is 5 wt % higher. The reason for this discrepancy is that we apply competitive devolatilization reactions. This means that an exact fit of the proximate analysis is not guaranteed. Instead, the relative fraction of char, tars, and non-condensable gases is dependent upon the heating rate, which is also in accordance with reality. Strictly speaking, the composition of the tars and non-condensable gases used in the simulations should therefore have been dependent upon the heating rate, but this has not been implemented in this work. Finally, to support the previous claim that the difference between elemental input and output is due to the competitive devolatilization reactions, we find by integrating the mass release over all particles in the fuel bed that the elemental release rate from the fuel bed equals the elemental output rate from the simulation. We have also checked for energy conservation of the simulations and found that the enthalpy imbalance is less than 0.5%.

By comparison of the left (B−) and right (B) panels in Figure 9, we see that the fluid temperature above the first part of the bed is lower for the smallest particles (case B−). This is because most oxygen going through the first wind box is used to convert char in the lower part of the bed for this case. The oxygen-depleted hot gas coming from the char conversion in the lower part of the bed provides heat to speed up the devolatilization process in the upper sections of the bed but leaves little oxygen for combustion of these volatiles. For the case with the larger particles (case B), a smaller fraction of oxygen is used for char conversion on the first part of the bed (as a result of lower mass transfer coefficients). This means that there is more oxygen available for combustion of the volatiles immediately above the bed, which explains the higher

https://doi.org/10.1021/acs.energyfuels.1c04204
Energy Fuels 2022, 36, 5852−5867

temperatures in this section. The temperature difference between the two cases is, however, even larger in the last part of the bed. The reason for this is that there is no char left to heat the primary air toward the end of the bed for case B−. This means that the fluid temperature in the last part of the bed is close to the temperature in the second wind box (∼700 K). The effect of this lower temperature on the overall temperature is low, however, because the mass flow rates in the second primary air inlet are much lower than in the first. As a result of the intense devolatilization at the first part of the bed for case B−, this case has a relatively large fraction of unburnt volatiles leaving the primary chamber. This is seen as the cold plume of gas in the upper left part of the temperature plot for case B− (left-hand panel of Figure 9).

Let us now plot the temperature in the fuel bed as a function of the position in the bed. As we compare the results for case B− (smaller particles) to the base case (case B), we see in the left panel of Figure 10 that the temperature is somewhat higher in the beginning of the bed for case B−. This is due to the fact that, because the bed ignites early, the conversion of char progresses faster for the smaller particles as a result of the higher mass transfer coefficient. Faster char conversion yields higher temperatures. We also see that, for case B+ (large particles), the temperature in the beginning of the bed is lower than that for case B, which is explained through the same reasoning. As we go to the end of the bed, we see that the smallest particles result in the lowest temperature. This is as expected from the discussion in the previous paragraph, namely, that the bed has been fully converted at the two last positions, such that there are no combustion processes to heat the air.

For the right panel of Figure 10, we see that, above the last part of the bed (at elevation 0.35 m above the grate), the temperatures in the primary combustion chamber vary widely between cases B+ and B on one hand and case B− on the other hand (see also Figure 9). The reason for this is once again that, this far down on the bed, the fuel has already been completely consumed for case B−. It is not known from the experiments at which position the fuel bed is fully converted, but it seems that it happens somewhere before the last measurement ports. In comparison now of the numerical results to the experimental measurements (dashed black line), we find that, except for the very first point in the bed, the experimental measurements fall within the range defined by the extremes of the numerical results.

5.2. Variable Fuel Particle Velocity. We now turn our attention to the cases where we vary the inlet velocity of the fuel particles and, hence, the bed velocity while keeping the fuel feeding rate unchanged. The velocity of the fuel particles at various locations along the bed is still a function of the particle diameter ratio, as given by eq 23. By comparison of the three panels in Figure 11, we see that the faster the bed is moving, the longer the particles move before they are devolatilized and the longer the fuel moves down the grate before all of the char is completely converted. This is not surprising because the process of char conversion is slow and faster bed velocity means lower residence time in the bed for the fuel particles. As noted before, the vast majority of the bed is still used for char conversion for all cases. The temperature along the bed for the cases with a variable bed velocity is shown in the left-hand panel of Figure 12. Here, we see that the temperature at the end of the bed is high for the cases with the highest bed velocity (cases A and B). This is clearly

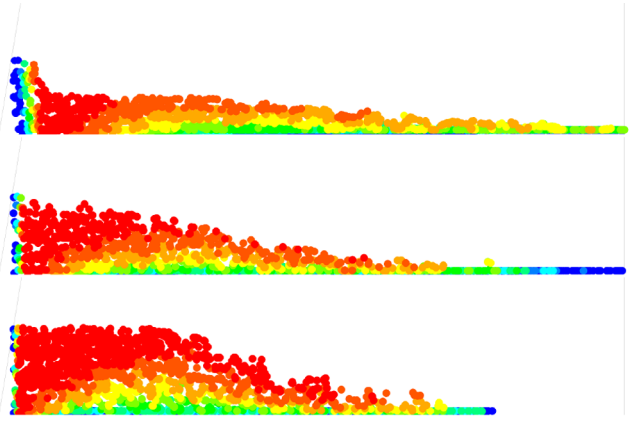

Figure 11. Particles in the fuel bed, color coded by mass of char, for cases (top) A, (middle) B, and (bottom) C. The color coding corresponds to the following fraction of the maximum mass of char: dark blue, <10%; green, ∼50%; and dark red, >90%.

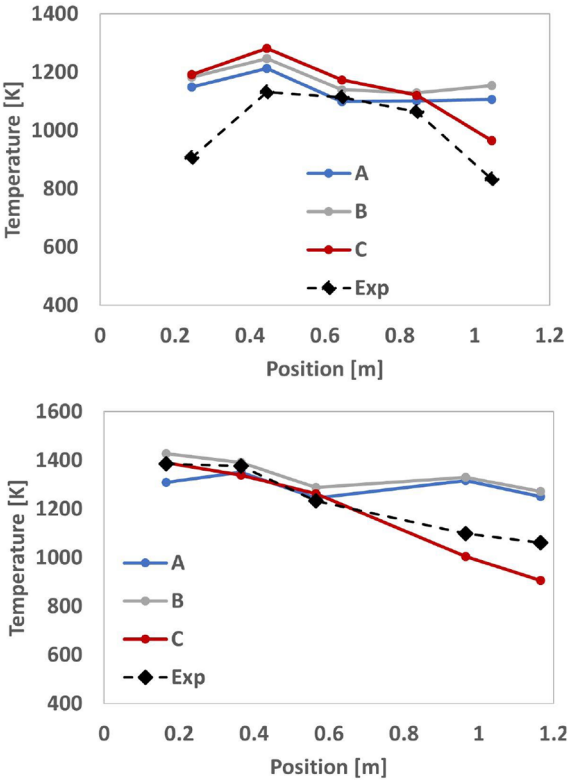

Figure 12. Temperature (top) along the fuel bed and (bottom) in the primary combustion chamber.

because these cases still have char left on the bed for the full extent of the grate, which means that the temperature of the bed is hot as a result of char conversion. The temperature for the case with low bed velocity (case C) follows a trend similar to the experiments, even though its temperature is consistently somewhat higher. This is most likely because the thermal conduction and radiation of the grate are not included. In the right-hand panel, which shows the temperature in the primary combustion chamber, we also see that case C reproduces the results from the experiments relatively well.

5.3. Variable Fuel Feeding Rate. It is interesting to investigate what the effect of the total fuel feeding rate is. From the experiment, a fuel feeding rate of 43.9 kg/h is reported,

https://doi.org/10.1021/acs.energyfuels.1c04204
Energy Fuels 2022, 36, 5852−5867

which is also what has been used in all of our simulations thus far. Now, we will lower the fuel feeding rate to 30.0 kg/h to see how this affects the results. The volume flow of air is kept unchanged. The first thing that we observe from Figure 13 is

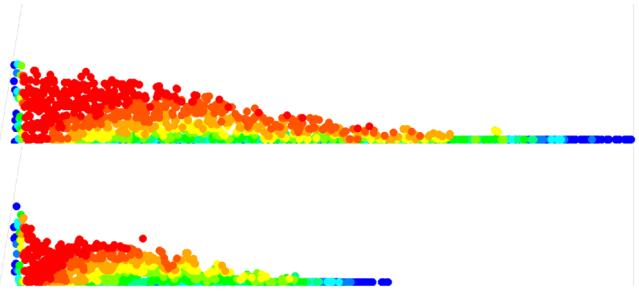

Figure 13. Particles in the fuel bed, color coded by mass of char, for cases (top) B and (bottom) BM−. The color coding corresponds to the following fraction of the maximum mass of char: dark blue, <10%; green, ∼50%; and dark red, >90%.

that the bed quickly reduces its height for the case with a lower fuel feeding rate. Then, we see that full burnout is observed slightly beyond halfway along the grate, which is much earlier than for the base case (case B). This is due to two effects: the first is that the air−fuel ratio in the bed is increased when lowering the fuel feeding rate, providing more oxygen for conversion of char, while the second is that a larger fraction of the fuel is accessible for radiative heating from above.

Looking now at Figure 14, we observe that the temperature is independent of the fuel feeding rate for the first three measurement points in the bed, although for the last two points, it is very different. This is because the bed is almost

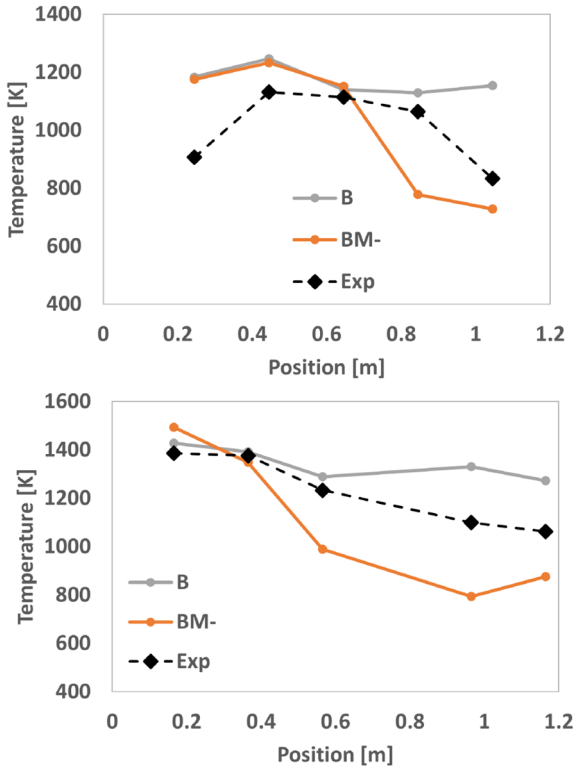

Figure 14. Temperature (top) along the fuel bed and (bottom) in the primary combustion chamber.

entirely consumed for case BM− this late on the grate. If we look above the bed in the primary chamber (right panel), the temperature is reduced already for the third measurement point. This is related to the fact that devolatilization ends earlier for the case with a low feeding rate, such that there are no volatile combustion in the gas phase at this point. It is interesting to note that, even with the lower heat input, a stable combustion is achieved. It is clear, however, that combustion will deteriorate significantly at some point as the feeding rate is reduced further.

6. CONCLUSION

In this paper, we present a transient bed model that is both detailed and computationally efficient. The coupling to ANSYS Fluent is also explained. The numerical framework is used to simulate a particular experimental test campaign performed at the pilot grate-firing facility of the University of Stuttgart. The results from the numerical simulations are compared to the experimental measurements from the test campaign.

In the simulations, we make the assumption that the grate can be modeled as a porous material with low conductivity and no influence on radiation. It turns out, however, that the temperature on the grate is sensitive to the way that the grate is treated in the simulations. As a matter of fact, the thermal conduction along the grate results in temperatures in the first part of the grate that are so high that the bed is ignited from below instead of from above. In the current two-dimensional setup, where it is not possible to handle the grate in an accurate manner, this is partly compensated by increasing the temperature of the primary air. Nevertheless, some differences between the numerical and experimental results are expected as a result of the numerical handling of the grate.

Because the wood chip fuel will have a certain particle size distribution and the shape of a typical wood chip cannot be accurately represented by our single-particle model, it is not obvious which particle size that is most appropriate to chose for our spherical representation of the fuel particles. In addition to this, an accurate value for the fuel inlet velocity is not clearly defined from the test campaign. Several simulations that cover a reasonable range of particle sizes (0.5−2 cm) and inlet bed velocities (0.4−1.6 mm/s) are therefore performed. For the properties that are of interest to this work, essentially all of the experimental results are within the error bars defined by the extremes in the numerical results. It is therefore concluded that, given well-defined inlet and initial properties, together with an accurate representation of the facility, the bed model should be able to predict the actual behavior of the real bed. As a result of the way the motion of the individual particles is calculated, which comes at a very low computational cost, the bed model has the potential to be used even in three-dimensional simulations of full-scale power plants.

APPENDIX

Temperature of Inner Boundaries

For a spherical particle, the temperature gradient in the radial direction is given as

$$\left.\frac{\mathrm{d}T}{\mathrm{d}r}\right|_{i,j} = \frac{T_i - T_j}{r_i(r_i/r_j - 1)} = \frac{T_j - T_i}{r_i(1 - r_i/r_j)} \tag{79}$$

Now, eq 38 is solved for $T_{b,3}$ using a fourth-order formula.

The energy balance at any interior boundary i is given by

https://doi.org/10.1021/acs.energyfuels.1c04204
Energy Fuels 2022, 36, 5852−5867

$$k_{p,i+1}A_{b,i}\left.\frac{dT}{dr}\right|_{bi,p(i+1)} - k_{p,i}A_{b,i}\left.\frac{dT}{dr}\right|_{bi,pi} - Q_{b,i} = 0 \quad (80)$$

The temperature at boundary i can therefore be expressed as

$$T_{b,i} = \frac{G_{bi,p(i+1)}T_{p,i+1} - G_{bi,pi}T_{p,i} + Q_{b,i}}{G_{bi,p(i+1)} - G_{bi,p(i)}} \quad (81)$$

when

$$G_{bi,pj} = \frac{r_{p,j}k_{p,j}A_{b,i}}{r_{b,i}(r_{b,i} - r_{p,j})} \quad (82)$$

and $Q_{b,i}$ is defined as the consumption rate as a result of the reactions at boundary i (i.e., it is positive if the boundary reactions consume energy, like, e.g., at the drying boundary).

Layer Temperature

The temperature of any given layer is increased by the heat that enters the layer from the outside, while it is decreased by the heat that leaves the layer toward the inside. This can be written as

$$\frac{dT_{p,i}}{dt} = \frac{\alpha_{p,i}}{V_{p,i}}\left(A_{b,i}\left.\frac{dT}{dr}\right|_{bi,pi} - A_{b,i-1}\left.\frac{dT}{dr}\right|_{b(i-1),pi}\right) \quad (83)$$

For the drying boundary, there is no thermal loss to inferior boundaries. The last term is therefore set to zero, i.e.

$$\frac{dT_{p,0}}{dt} = \frac{\alpha_{p,0}}{V_{p,0}}\left(A_{b,0}\left.\frac{dT}{dr}\right|_{b0,p0}\right) \quad (84)$$

Temperature of the Drying Boundary

In section 2.4.4, we show how the temperature of the drying boundary can be determined on the basis of the framework presented in the Temperature of Inner Boundaries section of the Appendix. Because we are in possession of F_{b0}, an alternative way of determining this temperature is to substitute eq 80 with

$$k_{p,1}A_{b,0}\left.\frac{dT}{dr}\right|_{b0,p1}(1 - F_{b0}) - k_{p,0}A_{b,0}\left.\frac{dT}{dr}\right|_{b0,p0} = 0 \quad (85)$$

We can now solve for $T_{b,0}$ to obtain

$$T_{b,0} = \frac{G_{b0,p1}(1 - F_{b0})T_{p,1} - G_{b0,p0}T_{p,0}}{G_{b0,p1}(1 - F_{b0}) - G_{b0,p0}} \quad (86)$$

The temperature of the boiling boundary cannot be higher than the boiling temperature. This is enforced by setting

$$T_{b,0} = \min(T_{b,0}, T_{boiling}) \quad (87)$$

where $T_{boiling}$ = 373 K.

AUTHOR INFORMATION

Corresponding Author

Nils Erland L. Haugen − *Department of Thermal Energy, SINTEF Energy Research, 7491 Trondheim, Norway;* orcid.org/0000-0002-9184-8722; Phone: +47-98608683; Email: nils.e.haugen@sintef.no

Authors

Mette Bugge − *Department of Thermal Energy, SINTEF Energy Research, 7491 Trondheim, Norway*

Alexander Mack − *Institute of Combustion and Power Plant Technology, Stuttgart University, 70569 Stuttgart, Germany*

Tian Li − *RISE Fire Research, 7092 Tiller, Norway; Department of Energy and Process Engineering, Norwegian University of Science and Technology, 7491 Trondheim, Norway;* orcid.org/0000-0002-4248-8396

Øyvind Skreiberg − *Department of Thermal Energy, SINTEF Energy Research, 7491 Trondheim, Norway;* orcid.org/0000-0001-6766-1282

Complete contact information is available at: https://pubs.acs.org/10.1021/acs.energyfuels.1c04204

Notes

The authors declare no competing financial interest.

ACKNOWLEDGMENTS

This research was supported by the GrateCFD Project (Grant 267957/E20), which is funded by LOGE AB, Statkraft Varme AS, EGE Oslo, Vattenfall AB, Hitachi Zosen Inova AG, and Returkraft AS together with the Research Council of Norway through the ENERGIX Program and by the CapeWaste Project (Grant 281869) funded by the Research Council of Norway through the CLIMIT Programme as well as the NUCA Project (Grant 0324342A) funded by the Federal Ministry for Economic Affairs and Energy of Germany.

REFERENCES

(1) Thunman, H.; Leckner, B.; Niklasson, F.; Johnsson, F. Combustion of wood particles—A particle model for Eulerian calculations. *Combust. Flame* **2002**, *129*, 30−46.

(2) Wissing, F.; Wirtz, S.; Scherer, V. Simulating municipal solid waste incineration with a DEM/CFD method—Influences of waste properties, grate and furnace design. *Fuel* **2017**, *206*, 638−656.

(3) Hermansson, S.; Thunman, H. CFD modelling of bed shrinkage and channelling in fixed-bed combustion. *Combust. Flame* **2011**, *158*, 988−999.

(4) Ström, H.; Thunman, H. CFD simulations of biofuel bed conversion: A submodel for the drying and devolatilization of thermally thick wood particles. *Combust. Flame* **2013**, *160*, 417−431.

(5) Gómez, M. A.; Porteiro, J.; De la Cuesta, D.; Patiño, D.; Míguez, J. L. Dynamic simulation of a biomass domestic boiler under thermally thick considerations. *Energy Conversion and Management* **2017**, *140*, 260−272.

(6) Shiehnejadhesar, A.; Mehrabian, R.; Hochenauer, C.; Scharler, R. The virtual biomass grate furnace-an overall CFD model for biomass combustion plants. *Energy Procedia* **2017**, *120*, 516−523.

(7) Barroso, G.; Roth, S.; Nussbaumer, T. Investigation of biomass conversion on a moving grate by pyrolysis gas analysis and fuel bed modelling. *Energy* **2019**, *174*, 897−910.

(8) Gu, T.; Yin, C.; Ma, W.; Chen, G. Municipal solid waste incineration in a packed bed: A comprehensive modeling study with experimental validation. *Applied Energy* **2019**, *247*, 127−139.

(9) Mehrabian, R.; Shiehnejadhesar, A.; Scharler, R.; Obernberger, I. Multi-physics modelling of packed bed biomass combustion. *Fuel* **2014**, *122*, 164−178.

(10) Zhang, J.; Li, T.; Ström, H.; Løvås, T. Computationally efficient coarse-graining XDEM/CFD modeling of fixed-bed combustion of biomass. *Combust. Flame* **2022**, *238*, 111876.

(11) Somwangthanaroj, S.; Fukuda, S. CFD modeling of biomass grate combustion using a steady-state discrete particle model (DPM) approach. *Renewable Energy* **2020**, *148*, 363−373.

(12) Khodaei, H.; Al-Abdeli, Y. M.; Guzzomi, F.; Yeoh, G. H. An overview of processes and considerations in the modelling of fixed-bed biomass combustion. *Energy* **2015**, *88*, 946−972.

(13) Dernbecher, A.; Dieguez-Alonso, A.; Ortwein, A.; Tabet, F. Review on modelling approaches based on computational fluid

dynamics for biomass combustion systems. *Biomass Convers. Biorefin.* **2019**, *9*, 129−182.
(14) Hosseini Rahdar, M.; Nasiri, F.; Lee, B. A Review of Numerical Modeling and Experimental Analysis of Combustion in Moving Grate Biomass Combustors. *Energy Fuels* **2019**, *33*, 9367−9402.
(15) Li, T.; Thunman, H.; Ström, H. A fast-solving particle model for thermochemical conversion of biomass. *Combust. Flame* **2020**, *213*, 117−131.
(16) Gunn, D. J. Transfer of heat or mass to particles in fixed and fluidized beds. *Int. J. Heat Mass Transfer* **1978**, *21*, 467−476.
(17) Haberle, I.; Skreiberg, O.; Lazar, J.; Haugen, N. E. L. Numerical models for thermochemical degradation of thermally thick woody biomass, and their application in domestic wood heating appliances and grate furnaces. *Prog. Energy Combust. Sci.* **2017**, *63*, 204−252.
(18) Haberle, I.; Haugen, N. E. L.; Skreiberg, O. Drying of thermally thick wood particles: A study of the numerical efficiency, accuracy, and stability of common drying models. *Energy Fuels* **2017**, *31*, 13743−13760.
(19) Razmjoo, N. Characterization of conversion zones in a reciprocating grate furnace firing wet woody biomass. Ph.D. Thesis, Linnaeus University, Vaxjo, Sweden, 2018.
(20) Westbrook, C. K.; Dryer, F. L. Simplified reaction mechanisms for the oxidation of hydrocarbon fuels in flames. *Combust. Sci. Technol.* **1981**, *27*, 31−43.

https://doi.org/10.1021/acs.energyfuels.1c04204
Energy Fuels 2022, 36, 5852−5867